bioRxiv preprint doi: https://doi.org/10.1101/054288; this version posted May 27, 2016. The copyright holder for this preprint (which was not certified by peer review) is the author/funder. All rights reserved. No reuse allowed without permission.

Top-down modulation of stimulus drive via beta-gamma cross-frequency interaction.

Craig G. Richter[1,5,*], William H. Thompson[1,2,5], Conrado A. Bosman[3,4] Pascal Fries[1,3,*]

[1] Ernst Strüngmann Institute (ESI) for Neuroscience in Cooperation with Max Planck Society, Deutschordenstraße 46, 60528 Frankfurt, Germany

[2] Department of Clinical Neuroscience , Karolinska Institute, Nobels Väg 9, 171 77 Solna, Sweden

[3] Donders Institute for Brain, Cognition and Behaviour, Kapittelweg 29, Radboud University, 6525 EN Nijmegen, Netherlands

[4] Swammerdam Institute for Life Sciences, Center for Neuroscience, Faculty of Science, University of Amsterdam, Sciencepark 904, 1098 XH Amsterdam, Netherlands

[5] Co-first authors

*Correspondence: craig.richter@esi-frankfurt.de, pascal.fries@esi-frankfurt.de

bioRxiv preprint doi: https://doi.org/10.1101/054288; this version posted May 27, 2016. The copyright holder for this preprint (which was not certified by peer review) is the author/funder. All rights reserved. No reuse allowed without permission.

SUMMARY

Recently, several studies have demonstrated that visual stimulus routing is subserved by inter-areal gamma-band synchronization, whereas top-down influences are mediated by alpha-beta band synchronization. These processes might implement top-down control, if top-down and bottom-up mediating rhythms are coupled through cross-frequency interaction. To test this possibility, we investigated Granger-causal influences among awake macaque primary visual area V1, higher visual area V4 and parietal control area 7a during attentional task performance. Top-down 7a-to-V1 beta-band influences enhanced visually driven V1-to-V4 gamma-band influences. This enhancement was spatially specific and largest for a beta-to-gamma delay of ~100 ms, suggesting a causal relationship. We propose that this cross-frequency interaction mechanistically subserves the attentional control of stimulus selection.

bioRxiv preprint doi: https://doi.org/10.1101/054288; this version posted May 27, 2016. The copyright holder for this preprint (which was not certified by peer review) is the author/funder. All rights reserved. No reuse allowed without permission.

INTRODUCTION

Many cognitive effects in vision can only be explained by invoking the concept of top-down influences (Gilbert and Sigman, 2007). For example, when top-down influences can pre-allocate attention to specific spatial locations, stimulus processing is more accurate and/or faster, even when stimuli remain unaltered. Correspondingly, neurons in early and mid-level visual cortex show enhanced firing rates when processing attended stimuli. These neurophysiological consequences of top-down control need to be mediated by corresponding projections. Indeed, anatomical studies have documented projections in the top-down direction that are at least as numerous as bottom-up projections. Bottom-up and top-down projections show different characteristic laminar patterns of origin and termination, and the pattern of pairwise projections abides by a global hierarchy, in which each area occupies a particular hierarchical level (Felleman and Van Essen, 1991; Hilgetag et al., 1996; Markov et al., 2014). Recently, it has been shown that the pattern of anatomical projections is closely correlated to a pattern of frequency-specific directed inter-areal influences. Influences mediated by bottom-up projections are primarily carried by gamma-band synchronization in both macaque and human visual cortex; by contrast, influences mediated by top-down projections are primarily carried by alpha-beta-band synchronization (Bastos et al., 2015b; Michalareas et al., 2016; van Kerkoerle et al., 2014). A similar association of higher frequency bands with bottom-up and lower frequency bands with top-down projections has been found also in the auditory system (Fontolan et al., 2014) and the hippocampus (Bieri et al., 2014; Colgin et al., 2009).

These relations between anatomy and physiology suggest that gamma rhythms are more involved in the bottom-up routing of stimulus information, whereas alpha-beta rhythms play a key role in modulating this process through top-down control (Bastos et al., 2012). In support of this, inter-areal gamma-band coherence is enhanced during tasks that involve primarily bottom-up stimulus routing (like pop-out), whereas inter-areal alpha-beta band coherence is enhanced during tasks that require top-down control (like visual search) (Buschman and Miller, 2007; von Stein et al., 2000). During sustained visual attention tasks, and probably also during much of natural viewing, top-down and bottom-up influences are both present simultaneously, with attentional top-down control persistently influencing bottom-up stimulus processing. The coexistence of both rhythms suggests the following scenario for attentional influences on visual processing: 1) Visual stimulation induces bottom-up gamma-band influences among visual areas; 2) Top-down beta-band influences are endogenously generated and thereby stimulus independent; 3) Attention enhances both, top-down beta-band and bottom-up gamma-band influences; 4) Cross-frequency interactions result in top-down beta-band influences enhancing subsequent bottom-up gamma-band influences in a spatially specific manner. There is substantial evidence for points 1) to 3), and this paper provides evidence for point 4). Regarding point 1): Gamma-band activity is induced by visual stimulation in lower visual areas (Gray et al., 1989) and it entrains gamma in higher visual areas in a bottom-up manner (Bastos et al., 2015b; Bosman et al., 2012; Grothe et al., 2012; Jia et al., 2013). Note that in higher visual areas, attention alone can induce gamma among local interneurons, and the projecting pyramidal cells join when visual stimulation commences (Vinck et al., 2013). Regarding point 2): Beta-band influences among visual areas are present before stimulus onset, and are typically stronger in the top-down direction (Bastos et al., 2015b; Bressler et al., 2007). Regarding point 3): Inter-areal gamma-band coherence and bottom-up gamma-band influences are enhanced by attention (Bosman et al., 2012; Grothe et al., 2012), and so are top-down beta-band influences (Bastos et al., 2015b). In the present study, we will confirm points 1) – 3) for ECoG data recorded from two macaque monkeys, when they direct attention to the contralateral versus ipsilateral hemifield. To investigate point 4), we then analyze spontaneous fluctuations in top-down beta-band and bottom-up gamma-band influences and their mutual interplay. We find that on a moment-by-moment basis, top-down beta-band influences correlate positively with bottom-up gamma-band influences. Spontaneous enhancements in top-down beta-band influences were followed ~100 ms later by enhancements in bottom-up gamma-band influences, suggestive of a causal relation. Consistent with a role in selective attention, this effect was spatially specific, i.e.

bioRxiv preprint doi: https://doi.org/10.1101/054288; this version posted May 27, 2016. The copyright holder for this preprint (which was not certified by peer review) is the author/funder. All rights reserved. No reuse allowed without permission.

bottom-up gamma-band influences depended most strongly on the top-down beta-band influences, that were directed to the origin of the bottom-up influence.

RESULTS

Top-down versus Bottom-up Spectral Asymmetries and their Stimulus and Task Dependence

To demonstrate that inter-areal gamma-band synchronization is stimulus driven (Bosman et al., 2012; Grothe et al., 2012), we first contrasted the pair-wise phase consistency (PPC), a frequency-resolved measure of synchronization (Vinck et al., 2010), between the fixation and stimulation conditions in two awake monkeys (monkey K and monkey P) (Figure 1A, C-F). We assessed the PPC between two region-of-interest (ROI) pairs: 7A-V1 and V1-V4 (Figure 1B). The ROI pair 7A-V1 (Figure 1K blue arrow) was selected, because it constitutes a clear top-down pathway from a very high-level control area to primary visual cortex (Bastos et al., 2015b; Michalareas et al., 2016). The ROI pair V1-V4 (Figure 1K green arrow) was selected, because it constitutes a clear bottom-up pathway emerging from V1, i.e. the area targeted by the top-down 7A→V1 influence. For both ROI pairs, the ECoG provided good coverage.

Figures 1C, E show, for monkey K, significantly enhanced gamma-band (~76 Hz) synchronization between ROI pairs V1-V4 and 7A-V1 once the stimulus has appeared, in contrast to an almost flat spectrum when no stimulus is present. This finding is consistent with gamma-band oscillations occurring as a result of stimulus drive. In contrast, beta-band (~17 Hz) synchronization for both ROI pairs is present already during the pre-stimulus fixation period, suggesting an endogenous origin (Figure 1C, E). Beta-band synchronization is maintained with slightly reduced strength during the stimulation period. These results were combined over both monkeys (Figure 1D, F) by aligning the peak beta and gamma oscillatory frequencies (PPC gamma peak frequency: monkey K: ~76 Hz, monkey P: ~65 Hz; PPC beta peak frequency: monkey K: ~17 Hz, monkey P: ~13 Hz). The combined data show the same pattern of results. Results for monkey P are shown in Figure S1.

We next assessed the dominant directionality of interareal synchronization and its attentional modulation. We quantified directionality of synchronization by means of Granger causality (GC) (Bressler and Seth, 2011; Ding et al., 2006; Granger, 1969). As shown by Bastos et al. (2015b), and extended to humans by Michalareas et al. (2016), the top-down beta-band influence of area 7A to V1 is significantly greater than the bottom-up beta-band influence of V1 to 7A. This holds for the example monkey K (Figure 1L; GC beta peak frequency: ~17 Hz) and the combined data (Figure 1M, GC beta peak frequency monkey P: ~12 Hz). This top-down beta-band influence is significantly increased when attention is directed to the visual hemifield contralateral to the recording grid (Figure 1G for monkey K, Figure 1H for both monkeys combined), consistent with an earlier report (Bastos et al., 2015a). Between V1 and V4, the gamma-band influence is stronger in the bottom-up direction from area V1 to V4 (Figure 1N for monkey K, GC gamma peak frequency: ~76 Hz; Figure 1O for both monkeys combined, GC gamma peak frequency of monkey P: ~65 Hz). The bottom-up gamma-band influence of V1 to V4 was significantly increased with attention (Figure 1I, J).

Top-down Beta Influences and Bottom-up Gamma Influences are Correlated Across Time

Endogenous increases in top-down beta GC may lead to an increase in stimulus-driven bottom-up gamma GC; therefore, we sought to determine whether the observed top-down beta GC and bottom-up gamma GC are consistent with such a scenario. Quantification of correlation between moment-by-moment co-fluctuations in two GC influences is normally precluded by the fact that GC influences are not defined per single data epoch (without substantially sacrificing spectral resolution and/or signal-to-noise ratio). To surmount this problem, we used the recently developed method of Jackknife Correlation (JC), which quantifies the correlation by first calculating GC influences for all leave-one-out subsamples (i.e. the jackknife replications of all epochs) and then correlating these values (Richter et al., 2015).

bioRxiv preprint doi: https://doi.org/10.1101/054288; this version posted May 27, 2016. The copyright holder for this preprint (which was not certified by peer review) is the author/funder. All rights reserved. No reuse allowed without permission.

Here we used JC to correlate the top-down GC from a 7A site to a V1 site with the bottom-up GC from the same V1 site to a V4 site. We refer to these configurations of three sites as 'triplets', and the JC was determined for all possible 7A→V1→V4 triplets (N=10664, Monkey K: 3944, Monkey P=6720). The JC was calculated between all possible combinations of top-down frequencies and bottom-up frequencies, both ranging from 1-100 Hz. Figure 2A shows the average over all triplets from monkey K. It reveals that top-down beta GC is correlated with bottom-up beta GC, and the same holds for the respective gamma GCs. Crucially, top-down beta GC also shows a significant positive correlation with bottom-up gamma GC. The peak of this cross-frequency interaction is well aligned with the average 7A→V1 beta and V1→V4 gamma GC peak frequencies (Figure 1A, line plots – intersection of the dashed lines). Importantly, there is no significant JC between 7A→V1 gamma and V1→V4 beta GC, even though 7A→V1 gamma GC is significantly correlated to V1→V4 gamma GC and 7A→V1 beta GC is significantly correlated to V1→V4 beta GC. Figure 2B confirms the same pattern of results after averaging over both monkeys, which entailed the alignment of their respective beta and gamma GC peaks. Results for monkey P are shown in Figure S1. Figure 2C shows a specific triplet selected from monkey K with a sizeable correlation coefficient of rho(2653) = 0.16 between 7A→V1 beta and V1→V4 gamma GC. Again, the area of maximal correlation is well aligned with the top-down beta and bottom-up gamma peak frequencies for this particular triplet. Thus, though the average level of correlation across triplets is relatively low, specific triplet correlations may fall between small to moderate size (Cohen, 1988).

We next investigated whether the JC between 7A→V1 beta and V1→V4 gamma GC depended on involving the same V1 site, which would demonstrate spatial specificity at the level of recording sites. We tested this spatial specificity by pairing 7A→V1 beta GC to a specific V1 site, with V1→V4 gamma GC from a different V1 site, where the distance that separated the two V1 sites was parametrically varied. Figure 3A shows for monkey K the boundaries of the recording grid and prominent sulci based on the monkey's MRI and surgical photographs. For each V1 site, 5 sets of other V1 sites were defined that fell into pre-specified distance intervals (1 cm per interval, stepped by 2.5 mm, between 0 and 2 cm). Figure 3A shows one example V1 site (arrow) and illustrates with 5 colored lines the five distance intervals (colored lines were slightly displaced for illustration purposes). The mean V1 distance for each distance interval is marked with a filled circle. Figure 3B shows the resulting JC computed for a ± 5 Hz frequency window around the peak 7A→V1 beta and V1→V4 gamma GC frequencies averaged over triplets and monkeys. It can be seen that as the distance between the two V1 sites increases from zero, there is a monotonic falloff of the correlation coefficient between 7A→V1 beta and V1→V4 gamma GC. This indicates that top-down beta and bottom-up gamma GC influences are not global, but rather are spatially specific, such that the correlation is maximal when the top-down beta GC influence is targeting the same V1 region that is projecting the bottom-up gamma GC influence. This is not trivially explained by GC calculation using the same V1 site, as explained in more detail in the discussion section.

Top-down Beta Influences Lead Bottom-up Gamma Influences in Time

We have established that spontaneous fluctuations in endogenous top-down beta GC are correlated with fluctuations in stimulus-driven bottom-up gamma GC. Yet, this does not demonstrate causality. Therefore, we investigated whether the data contain evidence in support of a causal relation, using a similar reasoning to GC, i.e. we assessed whether top-down beta GC is predictive of subsequent bottom-up gamma GC. To accomplish this, we extended the JC by adding a temporal dimension not dissimilar from time-lagged cross-correlation. We compute the JC on time-frequency data, where we systematically offset the data by positive or negative lags. We call this procedure lagged jackknife correlation (LJC). This quantifies at what time delay between the top-down beta-band influence and the bottom-up gamma-band influence the JC between them is largest. We computed LJC for each triplet. Figure 4A shows that the LJC, averaged over triplets of monkey K, peaked at -0.095 s, indicating that top-down beta GC leads bottom-up gamma GC by 0.095 s, and significantly differed from zero lag ($t(3943) = -3.438$, $p<<0.001$, two-tailed jackknife-based t-test). This relation was also

bioRxiv preprint doi: https://doi.org/10.1101/054288; this version posted May 27, 2016. The copyright holder for this preprint (which was not certified by peer review) is the author/funder. All rights reserved. No reuse allowed without permission.

present in monkey P, with top-down beta GC leading bottom-up gamma GC by 0.115 s (Figure 4B), and significantly differed from zero lag (t(6719) = -6.381, p<<0.001, two-tailed jackknife-based t-test). Figure 4C shows the LJC averaged over triplets and monkeys and exhibits a peak at -0.105 s (t(10663) = -7.576, p<<0.001, two-tailed jackknife-based t-test).

DISCUSSION

We used LFP recordings from 252-channel ECoG arrays covering large parts of the left hemispheres of two macaques to analyze the interaction between top-down and bottom-up GC influences. Top-down influences were quantified between area 7a at the top of the visual hierarchy (Bastos et al., 2015b; Markov et al., 2014) and V1 at the bottom. Bottom-up GC influences were quantified between V1 and V4, a known feedforward pathway carrying stimulus driven input (Bosman et al., 2012). Inter-areal top-down influences showed a beta-band peak, that was independent of visual stimulation and therefore endogenously generated, that was significantly larger in the top-down than the bottom-up direction, and that increased with selective attention. Bottom-up influences showed a gamma-band peak, that was stimulus driven, that was significantly larger in the bottom-up than the top-down direction, and that also increased with selective attention. Jackknife Correlation between top-down beta-band influences and bottom-up gamma-band influences revealed a cross-frequency interaction. This interaction was spatially specific, as it was maximal between top-down and bottom-up inter-areal influences that shared the same V1 site. Finally, top-down beta-band influences best predicted bottom-up gamma-band influences ~100 ms later, suggesting that the cross-frequency interaction is causal.

The Potential Influence of Noise

There are potential concerns related to the influence of noise. Noise can affect GC and it could thereby in principle affect the JC between GC fluctuations that we analyze here. One relevant scenario concerns noise that is shared between two signals, which can lead to artifactual GC (Nalatore et al., 2007; Vinck et al., 2015). Shared noise is typically due to volume conduction, which is strongly attenuated in our signals due to the bipolar derivation (Trongnetrpunya et al., 2015). Furthermore, artifactual GC alone does not lead to JC between GC, because the latter requires correlated GC fluctuations. GC fluctuations could in principle be due to fluctuations in shared noise. However, such noise influences on the two GC metrics would occur simultaneously and therefore, the lagged JC would peak at zero lag, whereas we found a lag of ~100 ms. Other influences of noise can be envisaged, and with sufficiently complex assumptions on multiple noise sources, essentially any correlation can be explained. The set of observations presented here, namely the fact that GC is correlated between different frequency bands, that this correlation shows high spatial specificity and in particular that the peak correlation occurs at a lag, would require assumptions that appear extremely implausible.

Correlation Magnitudes

Whereas noise is unlikely to explain the overall pattern of results, it might well influence the magnitude of observed correlations. The magnitude of correlations might be relevant to assess their functional significance. The JC for some triplets was at the level of rho ≈ 0.2, i.e. of moderate strength. However, the mean JC over all triplets tended towards a value an order of magnitude lower. This relatively low magnitude might be explained by uncorrelated noise. Uncorrelated physiological, measurement, and estimation noise will invariably lead to an underestimation of the true JC. These detrimental effects of noise are maximal for short data epochs and for correlations based on single trials, i.e. JC. Short data epochs, necessary to capture rapid fluctuations as the basis of our JC and LJC results, do not provide for the averaging out of stochastic physiological or measurement noise (Richter et al. (2015). JC across single trials, necessary for maximal sensitivity and fidelity, similarly reduces the correlation magnitude as compared to alternative approaches like sorting-and-binning that artificially inflate correlation magnitude (Richter et al. (2015).

bioRxiv preprint doi: https://doi.org/10.1101/054288; this version posted May 27, 2016. The copyright holder for this preprint (which was not certified by peer review) is the author/funder. All rights reserved. No reuse allowed without permission.

A Concrete Case of Cross-frequency Interaction

Numerous studies in visual cortex have reported gamma-band synchronization within and between visual areas (Bichot et al., 2005; Engel et al., 1991; Fries, 2001; Fries et al., 1997; Gray and Singer, 1989; Hoogenboom et al., 2006; Kreiter and Singer, 1996; Tallon-Baudry et al., 1996; Taylor et al., 2005; Womelsdorf et al., 2006; Wyart and Tallon-Baudry, 2008), and numerous studies in parietal cortex have reported beta-band synchronization within parietal areas and between parietal and frontal areas (Buschman and Miller, 2007; Dotson et al., 2014; Salazar et al., 2012; Stetson and Andersen, 2014). Recent ECoG recordings covering both visual and parietal areas revealed that inter-areal beta-band influences predominate in the top-down and inter-areal gamma-band influences predominate in the bottom-up direction (Bastos et al., 2015b). These findings link parietal beta-band activity with visual gamma-band activity and suggest a concrete case of cross-frequency interaction (Bressler and Richter, 2015). In the present paper, we have tested some of the resulting predictions and found direct experimental support for such a cross-frequency interaction that allows top-down beta-band influences to enhance bottom-up gamma-band influences.

Mechanisms

Cortical anatomy has revealed a distinct laminar pattern of top-down and bottom-up projections (Felleman and Van Essen, 1991; Markov et al., 2014). Bottom-up projections originate predominantly in superficial layers, and this predominance increases with the number of hierarchical levels bridged by the bottom-up projection. Furthermore, bottom-up projections terminate predominantly in layer 4. Top-down projections originate predominantly in deep layers, and this predominance increases with the number of hierarchical levels bridged by the top-down projection. Furthermore, top-down projections terminate predominantly outside layer 4, primarily in layers 1 and 6. Determining how the respective top-down influences interact with local processing and thereby ultimately with bottom-up influences remains a central neuroscientific quest. One potential mechanism has been proposed in a model that entails details of both layer-specific anatomy and cellular biophysics (Lee et al., 2013), and that replicates effects of top-down selective attention on bottom-up gamma-band coherence. The model implicates a subclass of inhibitory interneurons, the slow-inhibitory (SI) interneurons, as targets of top-down modulation. These cells may span multiple cortical laminae and thus are suitably situated for integration of neuronal activity across layers. A subpopulation of these cells, low-threshold spiking (LTS) cells, are found in deep layers of the cortex and are: 1) hypothesized to receive top-down input, 2) implicated in the generation of beta oscillations and in the resonant response to beta-rhythmic top-down input and 3) selectively modulate gamma band activation in layer 2/3, leading to an enhanced gamma band output. Our present analysis confirms the central prediction of the Lee et al. (2013) paper, namely that specifically top-down beta-band influences enhance stimulus-driven gamma-band processes. Lee et al. show how this mechanism can support the implementation of attentional stimulus selection. The current results, which mechanistically link the previously reported attentional enhancements of top-down beta and bottom-up gamma influences, provide the hitherto missing experimental bridge. Together, experiments, modeling and model-testing data analysis have led to an intriguingly coherent understanding of the neuronal processes behind the implementation of attentional stimulus selection.

EXPERIMENTAL PROCEDURES

Visual Stimulation and Behavioral Task

The experiment was approved by the ethics committee of the Radboud University Nijmegen (Nijmegen, The Netherlands). Two adult male macaque monkeys (monkey K and monkey P, both macaca mulatta) were used in this study. During experiments, monkeys were placed in a dimly lit booth facing a CRT monitor (120 Hz non-interlaced). When they touched a bar, a fixation point was presented, and gaze had to remain within the fixation window throughout the trial (monkey K: 0.85 deg radius, monkey P: 1 deg radius), otherwise the trial would be terminated and a new trial would commence. Once central fixation had been achieved and a subsequent 0.8 s pre-stimulus interval had

bioRxiv preprint doi: https://doi.org/10.1101/054288; this version posted May 27, 2016. The copyright holder for this preprint (which was not certified by peer review) is the author/funder. All rights reserved. No reuse allowed without permission.

elapsed, two isoluminant and isoeccentric drifting sinusoidal gratings were presented, one in each visual hemifield (diameter: 3 deg, spatial frequency: ~1 cycle/deg, drift velocity: ~1 deg/s, resulting temporal frequency: ~1 cycle/s, contrast: 100%). Blue and yellow tints were randomly assigned to each of the gratings on each trial (Figure 1A). Following a random delay interval (monkey K : 1 - 1.5 s; monkey P : 0.8 - 1.3 s), the central fixation point changed color to match one of the drifting gratings, indicating that this grating was the target stimulus, i.e. the fixation point color was the attentional cue. When the target stimulus was positioned in the visual hemifield contralateral to the recorded hemisphere, we refer to this condition as attend contra, whereas when the target was in the ipsilateral hemifield with respect to the ECoG grid, this condition is labeled attend ipsi. Either the target or distracter stimulus could undergo a subtle change in shape consisting of a transient bending of the bars of the grating (0.15 s duration of the full bending cycle). This change could occur at any monitor refresh from 0.75 s to 5 s (monkey K), and 4 s (monkey P) after stimulus onset. Bar releases within 0.15-0.5 s after target changes were rewarded. If stimulus changes occurred before the cue indicated which stimulus was the target, reports were rewarded in a random half of trials. Bar releases after distracter changes terminated the trial without reward. Trials were pooled from both contra and ipsi conditions, except where explicit comparisons of these conditions were made.

Neurophysiological Recordings

LFP recordings were made via a 252 channel electrocorticographic grid (ECoG) implanted subdurally over the left hemisphere (Rubehn et al., 2009). Data from the same animals, partly overlapping with the data used here, have been used in several previous studies (Bastos et al., 2015b; 2015a; Bosman et al., 2012; Brunet et al., 2015; 2014; Lewis et al., 2016; Pinotsis et al., 2014; Richter et al., 2015; Vinck et al., 2015). Recordings were sampled at approximately 32 kHz with a passband of 0.159 – 8000 Hz using a Neuralynx Digital Lynx system. The raw recordings were low-pass filtered to 250 Hz, and downsampled to 1 kHz. The electrodes were distributed over eight 32-channel headstages, and referenced against a silver wire implanted onto the dura overlying the opposite hemisphere. The electrodes were re-referenced via a bipolar scheme to achieve 1) greater signal localization 2) cancellation of the common reference, which could corrupt the validity of connectivity metrics, 3) to reject headstage specific noise. The bipolar derivation scheme subtracted the recordings from neighboring electrodes (spaced 2.5 mm) that shared a headstage, resulting in 218 bipolar derivations, henceforth referred to as “sites” (see Bastos et al. (2015b) for a detailed discussion of the re-referencing procedure). The site locations are shown as spheres in Figure 1B (monkey K: green, monkey P: black).

Three ROIs were selected for the current study: V1, V4, and area 7A (referred to simply as “7A”). ROIs were defined based on comparison of the electrode locations (co-registered to each monkey’s anatomical MRI and warped to the F99 template brain in CARET (Van Essen, 2012), with multiple cortical atlases of the macaque (see Bastos et al. (2015b) for a detailed discussion). Recording sites composing each ROI were co-registered to a common template (INIA19, (Rohlfing et al., 2012)), as were the Paxinos ROI definitions (Paxinos et al., 1999). The V1/V2 combined definition of Paxinos et al. (1999), is shown in Figure 1B/K (red) for simplicity due to uncertainty across atlases of the V1/V2 border, though recording site selection was based on multiple atlases with no recording sites selected that were believed to belong to area V2. Based on these ROI definitions, 77 recording sites were selected from area V1 (monkey K: 29, monkey P: 48), 31 from area V4 (monkey K: 17, monkey P: 14), and 18 from area 7A (monkey K: 8, monkey P: 10).

Preprocessing and Spectral Analysis General

Signal processing was conducted using the FieldTrip toolbox (Oostenveld et al., 2011). The raw data was line noise rejected via the subtraction of 50, 100, and 150 Hz components fit to the data using a discrete Fourier transform. Following trial epoching, specific to each analysis, epochs for each site were de-meaned. Epochs exceeding 5 standard deviations of all data from the same site in the same session were rejected. In addition, epochs were manually inspected and epochs with artifacts were

bioRxiv preprint doi: https://doi.org/10.1101/054288; this version posted May 27, 2016. The copyright holder for this preprint (which was not certified by peer review) is the author/funder. All rights reserved. No reuse allowed without permission.

rejected. The remaining epochs were normalized by the variance across all data in all epochs from the same site in the same recording session. Subsequently, all epochs were combined across sessions.

Spectral analysis was performed via the fast Fourier transform (FFT) on 0.5 s epochs. For frequencies from 0-50 Hz, a Hann taper was utilized, whereas for frequencies above 50 Hz, the multitaper method (MTM) was used to improve the spectral concentration of the gamma rhythm (Percival and Walden, 1993; Thomson, 1982). We applied 5 tapers, resulting in a spectral smoothing of +/- 6 Hz. All epochs were zero-padded to 1 s resulting in a spectral resolution of 1 Hz. The coefficients resulting from the FFT were used to determine the cross spectral density, which is the basis for two connectivity metrics employed: pairwise phase consistency (PPC) (Vinck et al., 2010), and Granger causality (GC) (Bressler and Seth, 2011; Granger, 1969). When GC is computed from the cross-spectral density, this is known as a non-parametric approach in contrast to the traditional parametric method based on autoregressive modeling (Dhamala et al., 2008). Connectivity metrics were computed between all inter-areal pairings of sites between ROIs: V1-V4, and V1-7A.

High Resolution Spectral Comparisons

For the analyses of Figure 1, we used all 0.5 s epochs that could be defined with 60% overlap. This overlap allows for the application of Welch's method (Welch, 1967) and was selected as an optimal overlap for the multitaper method, while maintaining a reasonable computational load (Percival and Walden, 1993; Thomson, 1977) For the analysis of stimulation versus fixation, each trial was segmented into a fixation and stimulation period. The fixation period was defined as the 0.5 s prior to stimulus onset, while the stimulation period was defined from 0.3 s post-stimulus onset (to avoid onset related transients) until the first of three possible events 1) the onset of the cue, 2) a change in the distracter stimulus, or 3) a change in the target stimulus. This resulted in 6822 fixation epochs (Monkey K: 3384, Monkey P: 3438) and 13675 stimulation epochs (Monkey K: 8109, Monkey P: 5566). Fixation versus stimulation was only compared for PPC, which inherently controls for sample size bias, thus no adjustments needed to be made to the large disparity in the number of trials between the fixation and stimulation conditions. Statistical assessment of the within-subject difference between fixation and stimulation conditions employed a non-parametric technique (Maris and Oostenveld, 2007) that inherently controls for multiple comparisons, where epochs were pooled and then randomly distributed between the fixation and stimulation conditions. FFT was then performed, followed by PPC. The difference between conditions was then computed, with the maximum absolute difference across the frequencies retained. This critical step ensures that the statistical test is corrected for multiple comparisons across the frequency dimension. The procedure was repeated 1000 times, forming a distribution of surrogate values against which the empirical values at each frequency may be compared. Group statistics were performed on the peak-aligned data by first averaging over all site pairs within-subject, and then averaging these results across the monkeys. This ensured that each monkey contributed equally to the overall result, despite having different numbers of site pairs. This averaging procedure was performed for each permutation, followed by the same max-based multiple-comparison correction. This gives rise to a surrogate distribution of data against which the group data may be assessed. Multiple comparisons correction was performed across all frequencies tested (1-45 Hz and 55-100 Hz in steps of 1 Hz).

To compare attention to the hemifield contralateral ("attend contra") versus ipsilateral ("attend ipsi") to the recorded hemisphere, we defined the post-cue period as the time from 0.3 s after cue presentation (to avoid cue presentation transients) until the first change in either the target or distracter stimulus. This period was segmented into as many 0.5 s epochs as possible with 60 % overlap. This resulted in 8313 attend contra epochs (Monkey K: 3819, Monkey P: 4494) and 7899 attend ipsi epochs (Monkey K: 3456, Monkey P: 4443), i.e. a total of 16212 attend epochs (Monkey K: 7275, Monkey P: 8937). Non-parametric GC is known to be biased by sample size (Bastos and Schoffelen, 2015), thus the number of epochs per attention condition needed to be balanced for each monkey. This was accomplished by finding the condition with the fewest epochs, and randomly selecting this number of

bioRxiv preprint doi: https://doi.org/10.1101/054288; this version posted May 27, 2016. The copyright holder for this preprint (which was not certified by peer review) is the author/funder. All rights reserved. No reuse allowed without permission.

epochs from the other condition. The statistical difference between conditions was also assessed using a non-parametric statistical framework as described for the fixation versus stimulation contrast.

The comparison of top-down versus bottom-up GC was performed on the pooled data from the attend contra and ipsi conditions. Since this was a within-condition comparison, no balancing of epoch numbers was needed, and all epochs from both attend conditions were used. The statistical analysis of the difference between top-down and bottom-up GC could not be obtained using a non-parametric randomization framework, because top-down and bottom-up GC are not properties of specific sets of epochs, but rather are expressed by all trials simultaneously. Therefore, an alternative statistical approach was used, namely the bootstrap (Efron and Tibshirani, 1994). Like with the randomization approach, the statistic of interest – in this case the top-down/bottom-up GC difference – is recomputed on each bootstrap resample, giving rise to a distribution of surrogate values. Following Efron and Tibshirani (1994), a confidence interval can be constructed from the surrogate distribution. To assess the statistical significance at p=0.05 (two-tailed), we find the 2.5th and 97.5th percentile values from the surrogate distribution of differences between top-down and bottom-up GC. This naturally forms the 95% confidence interval such that if zero lies outside of this interval, we may conclude that the result is significant at a level of p=0.05. This method does not control for multiple comparisons, but we can easily modify it to do so using the same logic employed by Maris and Oostenveld (2007). We performed 1000 bootstrap resamples. For each resample we determined the absolute difference across frequencies between the bootstrap resample spectrum and the average of all bootstrap resamples, and retained the maximum of this value across frequencies. Thus we are guaranteed to form the largest confidence interval possible across frequencies and in so doing construct an omnibus confidence interval that controls for the multiple comparisons. This confidence interval is applied to each frequency, and where it does not contain zero, the result is significant at p=0.05. To conduct group level statistics, the omnibus statistic is derived from the mean of each bootstrap resample of the difference between top-down and bottom-up spectra across both monkeys (first averaged within-subject across pairs), such that the mean of the empirical difference across the monkeys can be assessed for significance.

Jackknife Correlation

We aimed at quantifying the correlation between moment-by-moment co-fluctuations in two GC influences. This is normally precluded by the fact that GC influences are not defined per single data epoch (without substantially sacrificing spectral resolution and/or signal-to-noise ratio). Therefore, we used the Jackknife Correlation (JC), which quantifies the correlation by first calculating GC influences for all leave-one-out subsamples (i.e. the jackknife replications of all epochs) and then correlating these values (Richter et al., 2015). For each leave-one-out subsample, the GC or any other smooth function F of the data can be defined as follows:

$$F_{x_j} = F\left(x_1, x_2, \ldots, x_{j-1}, x_{j+1}, \ldots, x_n\right) \tag{1}$$

, where x specifies the recording site and j specifies the index of the left-out observation, here the epoch. JC requires independent epochs. Thus, we followed the same segmentation strategy as for the comparison of the attend conditions, but with zero overlap, which resulted in fewer epochs, totaling 6414 (Monkey K: 2655, Monkey P: 3759). Contra and ipsi conditions were combined for the JC analysis. The JC is defined using the following formula:

$$JC_{F_x F_y} = \frac{1}{n-1}\sum_{j=1}^{n}\left(\frac{F_{x_j} - \overline{F_x}}{s_{F_x}}\right)\left(\frac{F_{y_j} - \overline{F_y}}{s_{F_y}}\right) \tag{2}$$

bioRxiv preprint doi: https://doi.org/10.1101/054288; this version posted May 27, 2016. The copyright holder for this preprint (which was not certified by peer review) is the author/funder. All rights reserved. No reuse allowed without permission.

, where n is defined as the number of jackknife replications and is equal to the total number of epochs, F_{x_j} and F_{y_j} are the jackknife replications, $\overline{F_x}$ and $\overline{F_y}$ are the means of the jackknife replications, and s_{F_x} and s_{F_y} are the standard deviations of the jackknife replications. To use the JC with the Spearman correlation metric, we applied the above formula on the ranks of F_{x_j} and F_{y_j}.

For statistical testing, we created a distribution of 1000 JC values under a realization of the null hypothesis of independence between 7A→V1 and V1→V4 GC influences. This was realized by calculating JC between randomly permuted jackknife replications of 7A→V1 and V1→V4 GC influences. This is equivalent to calculating the JC between GC influences after leaving out a random epoch for the 7A→V1 GC and a random epoch for the V1→V4 GC without replacement. To control for multiple comparisons across the frequency-frequency combinations, the max-based approach (see above) was again employed, where for each permutation the maximum absolute Spearman's rho value was selected, giving rise to an omnibus distribution of surrogate correlation coefficients for each triplet. For maps showing the average correlation across triplets, this max-based method was performed on the mean over triplets, where for a given permutation each triplet was randomized in the same order as all others. This was done individually per monkey and after averaging across the two monkeys. When monkeys were combined, spectra were aligned to the beta- and gamma-peak frequencies and averages were first taken across all triplets of each monkey to weight both monkeys equally.

For testing spatial specificity, we analyzed recording site triplets, which did not share the same V1 site (see main text for details): 7A→$V1_a$$V1_b$→V4. Since a vast number of such triplets exist, yet we wished to select a number equal to the original number of triplets to control potential statistical bias, we selected a unique number of 7A→$V1_a$$V1_b$→V4 triplets that matched the original number of 7A→V1→V4 triplets evaluated for each monkey and then the performed the same JC procedure. To smooth the result statistically (exploring the large space of possibilities), we repeated this procedure 100 times, resulting in unique selections of V1 sites for each distance interval, and averaged the outcomes. Results were plotted against the average distance obtained for each distance interval.

Lagged Jackknife Correlation (LJC)

We used the jackknife correlation (JC) to quantify the correlation between top-down beta GC and bottom-up gamma GC. To this end, we left out one data epoch at a time, calculated GC influences, and determined the correlation between the resulting GC influences across all leave-one-out (jackknife) replications. Since a given jackknife replication eliminated the same epoch for the calculation of both GC influences, this established the correlation at zero time lag. Next, we were interested in whether the correlation depends on the time lag. To test this, we computed JC between GC influences calculated from epochs offset by a variable lag. The epochs were stepped at t intervals of 5 ms. The offsets were stepped at τ intervals of 5 ms. Note that stepping of intervals and offsets was in principle independent and could have been different, but it was chosen to be identical to speed up computation. We refer to this as lagged JC (LJC):

$$LJC_{F_xF_y}(\tau) = \frac{1}{n-1}\sum_{j=1}^{n}\left(\frac{F_{x_{j,t}} - \overline{F_x}}{s_{F_{x_t}}}\right)\left(\frac{F_{y_{j,t+\tau}} - \overline{F_y}}{s_{F_{y_{t+\tau}}}}\right) \quad (3)$$

τ was chosen to cover a range of lags from -500 ms to 500 ms. The GC calculation itself was as in the previous zero-lag JC, using 500 ms and the tapering specified above. We used data from 0.3 s post-cue to 2 s post-cue, eliminating shorter trials so that longer lags could be tested (878 trials used, Monkey K: 398, Monkey P: 480). LJC was calculated across trials, i.e. leaving out an entire trial at a

bioRxiv preprint doi: https://doi.org/10.1101/054288; this version posted May 27, 2016. The copyright holder for this preprint (which was not certified by peer review) is the author/funder. All rights reserved. No reuse allowed without permission.

time (this is different from the previous zero-lag JC, which used multiple non-overlapping epochs per trial if available). The data that was available per trial allowed for multiple realizations of the two epochs with a particular lag. For each lag, LJC was calculated separately for all possible realizations and averaged. The number of possible realizations decreases as the lag between top-down beta GC and bottom-up gamma GC increases, resulting in fewer LJC computations that are averaged. This results in a noisier estimate at larger lags, but no systematic bias in the mean JC value. The number of epochs that each LJC is computed upon always equals the number of trials. Formally, this implementation of the LJC is defined as:

$$LJC_{F_xF_y}(\tau) = \frac{1}{m-\tau}\sum_{t=1}^{m-\tau}\left[\frac{1}{n-1}\sum_{j=1}^{n}\left(\frac{F_{x_{j,t}} - \bar{F}_{x_t}}{s_{F_{x_t}}}\right)\left(\frac{F_{y_{j,t+\tau}} - \bar{F}_{y_{t+\tau}}}{s_{F_{y_{t+\tau}}}}\right)\right] \quad (4)$$

, where m is the number of 500 ms windows, stepped at 5 ms, that fitted into the trial length of 1.7 s.

Statistical significance was assessed using the same logic as used for the JC, where the epoch order of one member of the JC was permuted with respect to the other. For the LJC, the permutation was identical for each time step and lag, to be conservative. Multiple comparison correction must take place over the multiple lags, which is achieved by taking the maximum absolute Spearman's rho value across lags for each permutation. The resulting distribution is used to assess the probability that the empirical result at each lag occurred by chance. The empirical and the permutation metrics were first averaged over all triplets per monkey and then averaged over the two monkeys, to give equal weight to both subjects.

We wished to assess whether the LJC peak lag of -105 ms was significantly different from a lag of zero. We did so using a jackknife method to determine the standard error of the peak position in milliseconds (Efron, 1981). In this case we leave out a specific triplet to assess the variability of the peak. The jackknife procedure causes a compression of the variance (Richter et al., 2015), thus the 5 ms sampling grid would not be sufficient to represent the peak positions of the jackknife replications. To account for this, we cubic spline interpolated each replication to a resolution of 0.001 ms, which proved adequate to represent the variance of the peak. The peak of each jackknife replication was found using a Gaussian fit of the smoothed correlation as a function of lag (findpeaksG.m by T.C O'Haver). We then derived the standard error of the estimator, and converted this to a t-score by dividing the mean peak lag value of the jackknife replications by the estimated standard error. The significance of this t-value was then assessed against Student's t-distribution. At the group level, this procedure entails concatenating the data from both monkeys, and leaving out each triplet once. Based on this group estimate of the standard error, a t-value is derived, as above, and assessed for statistical significance.

bioRxiv preprint doi: https://doi.org/10.1101/054288; this version posted May 27, 2016. The copyright holder for this preprint (which was not certified by peer review) is the author/funder. All rights reserved. No reuse allowed without permission.

AUTHOR CONTRIBUTIONS

Conceptualization, C.G.R., W.H.T., C.A.B., and P.F.; Methodology, C.G.R., W.H.T., C.A.B., and P.F.; Software, C.G.R. and W.H.T.; Formal Analysis, C.G.R. and W.H.T.; Investigation, C.A.B. and P.F.; Writing – Original Draft, C.G.R. and P.F.; Writing – Review & Editing, C.G.R., W.H.T., C.A.B., and P.F.; Visualization, C.G.R.; Supervision, P.F.; Funding Acquisition, P.F.

ACKNOWLEDGMENTS

We would like to thank J. Vezoli for his assistance in ROI definition, co-registration and construction of anatomical renderings. This work was supported by DFG (SPP 1665, FOR 1847, FR2557/5-1-CORNET), EU (HEALTH-F2-2008-200728-BrainSynch, FP7-604102-HBP), a European Young Investigator Award, National Institutes of Health (1U54MH091657-WU-Minn-Consortium-HCP), the LOEWE program (NeFF) and an NWO-FLAG-ERA Joint Transnational Call 2015 (CAB).

REFERENCES

Bastos, A.M., Litvak, V., Moran, R., Bosman, C.A., Fries, P., Friston, K.J., (2015a). A DCM study of spectral asymmetries in feedforward and feedback connections between visual areas V1 and V4 in the monkey. Neuroimage 108, 460–475.

Bastos, A.M., Schoffelen, J.-M., (2015). A Tutorial Review of Functional Connectivity Analysis Methods and Their Interpretational Pitfalls. Front. Syst. Neurosci. 9, 175.

Bastos, A.M., Usrey, W.M., Adams, R.A., Mangun, G.R., Fries, P., Friston, K.J., (2012). Canonical microcircuits for predictive coding. Neuron 76, 695–711.

Bastos, A.M., Vezoli, J., Bosman, C.A., Schoffelen, J.-M., Oostenveld, R., Dowdall, J.R., De Weerd, P., Kennedy, H., Fries, P., (2015b). Visual areas exert feedforward and feedback influences through distinct frequency channels. Neuron 85, 390–401.

Bichot, N.P., Rossi, A.F., Desimone, R., (2005). Parallel and serial neural mechanisms for visual search in macaque area V4. Science 308, 529–534.

Bieri, K.W., Bobbitt, K.N., Colgin, L.L., (2014). Slow and fast γ rhythms coordinate different spatial coding modes in hippocampal place cells. Neuron 82, 670–681.

Bosman, C.A., Schoffelen, J.-M., Brunet, N., Oostenveld, R., Bastos, A.M., Womelsdorf, T., Rubehn, B., Stieglitz, T., De Weerd, P., Fries, P., (2012). Attentional Stimulus Selection through Selective Synchronization between Monkey Visual Areas. Neuron 75, 875–888.

Bressler, S.L., Richter, C.G., (2015). Interareal oscillatory synchronization in top-down neocortical processing. Curr. Opin. Neurobiol. 31, 62–66.

Bressler, S.L., Richter, C.G., Chen, Y., Ding, M., (2007). Cortical functional network organization from autoregressive modeling of local field potential oscillations. Stat. Med. 26, 3875–3885.

Bressler, S.L., Seth, A.K., (2011). Wiener-Granger causality: a well established methodology. Neuroimage 58, 323–329.

Brunet, N., Bosman, C.A., Roberts, M., Oostenveld, R., Womelsdorf, T., De Weerd, P., Fries, P., (2015). Visual Cortical Gamma-Band Activity During Free Viewing of Natural Images. Cereb. Cortex 25, 918–926.

Brunet, N.M., Bosman, C.A., Vinck, M., Roberts, M., Oostenveld, R., Desimone, R., De Weerd, P., Fries, P., (2014). Stimulus repetition modulates gamma-band synchronization in primate visual cortex. Proc. Natl. Acad. Sci. USA 111, 3626–3631.

Buschman, T.J., Miller, E.K., (2007). Top-down versus bottom-up control of attention in the prefrontal and posterior parietal cortices. Science 315, 1860–1862.

Cohen, J., (1988). Statistical Power Analysis for the Behavioral Sciences. Lawrence Erlbaum Associates.

Colgin, L.L., Denninger, T., Fyhn, M., Hafting, T., Bonnevie, T., Jensen, O., Moser, M.-B., Moser, E.I., (2009). Frequency of gamma oscillations routes flow of information in the

bioRxiv preprint doi: https://doi.org/10.1101/054288; this version posted May 27, 2016. The copyright holder for this preprint (which was not certified by peer review) is the author/funder. All rights reserved. No reuse allowed without permission.

hippocampus. Nature 462, 353–357.
Dhamala, M., Rangarajan, G., Ding, M., (2008). Analyzing information flow in brain networks with nonparametric Granger causality. Neuroimage 41, 354–362.
Ding, M., Chen, Y., Bressler, S.L., (2006). Granger Causality: Basic Theory and Application to Neuroscience. Handbook of Time Series Analysis: Recent Theoretical Developments and Applications.
Dotson, N.M., Salazar, R.F., Gray, C.M., (2014). Frontoparietal correlation dynamics reveal interplay between integration and segregation during visual working memory. J. Neurosci. 34, 13600–13613.
Efron, B., (1981). Nonparametric estimates of standard error: The jackknife, the bootstrap and other methods. Biometrika.
Efron, B., Tibshirani, R.J., (1994). An Introduction to the Bootstrap. CRC Press, Boca Raton.
Engel, A.K., Kreiter, A.K., König, P., Singer, W., (1991). Synchronization of oscillatory neuronal responses between striate and extrastriate visual cortical areas of the cat. Proc. Natl. Acad. Sci. USA 88, 6048–6052.
Felleman, D., Van Essen, D.C., (1991). Distributed hierarchical processing in the primate cerebral cortex. Cereb. Cortex 1, 1–47.
Fontolan, L., Morillon, B., Liegeois-Chauvel, C., Giraud, A.-L., (2014). The contribution of frequency-specific activity to hierarchical information processing in the human auditory cortex. Nat. Commun. 5, 4694.
Fries, P., (2001). Modulation of Oscillatory Neuronal Synchronization by Selective Visual Attention. Science 291, 1560–1563.
Fries, P., Roelfsema, P.R., Engel, A.K., König, P., Singer, W., (1997). Synchronization of oscillatory responses in visual cortex correlates with perception in interocular rivalry. Proc. Natl. Acad. Sci. USA 94, 12699–12704.
Gilbert, C.D., Sigman, M., (2007). Brain states: top-down influences in sensory processing. Neuron 54, 677–696.
Granger, C., (1969). Investigating causal relations by econometric models and cross-spectral methods. Econometrica 37, 424–438.
Gray, C.M., König, P., Engel, A.K., Singer, W., (1989). Oscillatory responses in cat visual cortex exhibit inter-columnar synchronization which reflects global stimulus properties. Nature 338, 334–337.
Gray, C.M., Singer, W., (1989). Stimulus-specific neuronal oscillations in orientation columns of cat visual cortex. Proc. Natl. Acad. Sci. USA 86, 1698–1702.
Grothe, I., Neitzel, S.D., Mandon, S., Kreiter, A.K., (2012). Switching neuronal inputs by differential modulations of gamma-band phase-coherence. J. Neurosci. 32, 16172–16180.
Hilgetag, C.C., O'Neill, M.A., Young, M.P., (1996). Indeterminate organization of the visual system. Science 271, 776–777.
Hoogenboom, N., Schoffelen, J.-M., Oostenveld, R., Parkes, L.M., Fries, P., (2006). Localizing human visual gamma-band activity in frequency, time and space. Neuroimage 29, 764–773.
Jia, X., Tanabe, S., Kohn, A., (2013). Gamma and the Coordination of Spiking Activity in Early Visual Cortex. Neuron 77, 762–774.
Kreiter, A.K., Singer, W., (1996). Stimulus-dependent synchronization of neuronal responses in the visual cortex of the awake macaque monkey. J. Neurosci. 16, 2381–2396.
Lee, J.H., Whittington, M.A., Kopell, N.J., (2013). Top-down beta rhythms support selective attention via interlaminar interaction: a model. PLoS Comput. Biol. 9, e1003164.
Lewis, C.M., Bosman, C.A., Womelsdorf, T., Fries, P., (2016). Stimulus-induced visual cortical networks are recapitulated by spontaneous local and interareal synchronization. Proc. Natl. Acad. Sci. USA 113, E606–15.
Maris, E., Oostenveld, R., (2007). Nonparametric statistical testing of EEG- and MEG-data. J. Neurosci. Methods 164, 177–190.
Markov, N.T., Vezoli, J., Chameau, P., Falchier, A., Quilodran, R., Huissoud, C., Lamy, C.,

bioRxiv preprint doi: https://doi.org/10.1101/054288; this version posted May 27, 2016. The copyright holder for this preprint (which was not certified by peer review) is the author/funder. All rights reserved. No reuse allowed without permission.

Misery, P., Giroud, P., Ullman, S., Barone, P., Dehay, C., Knoblauch, K., Kennedy, H., (2014). Anatomy of hierarchy: feedforward and feedback pathways in macaque visual cortex. J. Comp. Neurol. 522, 225–259.

Michalareas, G., Vezoli, J., van Pelt, S., Schoffelen, J.-M., Kennedy, H., Fries, P., (2016). Alpha-Beta and Gamma Rhythms Subserve Feedback and Feedforward Influences among Human Visual Cortical Areas. Neuron 89, 384–397.

Oostenveld, R., Fries, P., Maris, E., Schoffelen, J.-M., (2011). FieldTrip: Open source software for advanced analysis of MEG, EEG, and invasive electrophysiological data. Comput. Intell. Neurosci. 2011, 156869.

Paxinos, G., Huang, X., Toga, A.W., (1999). The Rhesus Monkey Brain in Stereotaxic Coordinates. Academic Press, San Diego.

Percival, D.B., Walden, A.T., (1993). Spectral Analysis for Physical Applications. Cambridge University Press.

Pinotsis, D.A., Brunet, N., Bastos, A., Bosman, C.A., Litvak, V., Fries, P., Friston, K.J., (2014). Contrast gain control and horizontal interactions in V1: A DCM study. Neuroimage 92, 143–155.

Richter, C.G., Thompson, W.H., Bosman, C.A., Fries, P., (2015). A jackknife approach to quantifying single-trial correlation between covariance-based metrics undefined on a single-trial basis. Neuroimage 114, 57–70.

Rohlfing, T., Kroenke, C.D., Sullivan, E.V., Dubach, M.F., Bowden, D.M., Grant, K.A., Pfefferbaum, A., (2012). The INIA19 Template and NeuroMaps Atlas for Primate Brain Image Parcellation and Spatial Normalization. Front. Neuroinform. 6, 27.

Rubehn, B., Bosman, C., Oostenveld, R., Fries, P., Stieglitz, T., (2009). A MEMS-based flexible multichannel ECoG-electrode array. J. Neural. Eng. 6, 036003.

Salazar, R.F., Dotson, N.M., Bressler, S.L., Gray, C.M., (2012). Content-specific fronto-parietal synchronization during visual working memory. Science 338, 1097–1100.

Stetson, C., Andersen, R.A., (2014). The parietal reach region selectively anti-synchronizes with dorsal premotor cortex during planning. J. Neurosci. 34, 11948–11958.

Tallon-Baudry, C., Bertrand, O., Delpuech, C., Pernier, J., (1996). Stimulus specificity of phase-locked and non-phase-locked 40 Hz visual responses in human. J. Neurosci. 16, 4240–4249.

Taylor, K., Mandon, S., Freiwald, W.A., Kreiter, A.K., (2005). Coherent oscillatory activity in monkey area v4 predicts successful allocation of attention. Cereb. Cortex 15, 1424–1437.

Thomson, D.J., (1982). Spectrum estimation and harmonic analysis. Proceedings of the IEEE 70, 1055–1096.

Thomson, D.J., (1977). Spectrum Estimation Techniques for Characterization and Development of WT4 Waveguide-I. Bell System Technical Journal 56, 1769–1815.

Trongnetrpunya, A., Nandi, B., Kang, D., Kocsis, B., Schroeder, C.E., Ding, M., (2015). Assessing Granger Causality in Electrophysiological Data: Removing the Adverse Effects of Common Signals via Bipolar Derivations. Front. Syst. Neurosci. 9, 189.

Van Essen, D.C., (2012). Cortical cartography and Caret software. Neuroimage 62, 757–764.

van Kerkoerle, T., Self, M.W., Dagnino, B., Gariel-Mathis, M.-A., Poort, J., van der Togt, C., Roelfsema, P.R., (2014). Alpha and gamma oscillations characterize feedback and feedforward processing in monkey visual cortex. Proc. Natl. Acad. Sci. USA 111, 14332–14341.

Vinck, M., Huurdeman, L., Bosman, C.A., Fries, P., Battaglia, F.P., Pennartz, C.M.A., Tiesinga, P.H., (2015). How to detect the Granger-causal flow direction in the presence of additive noise? Neuroimage 108, 301–318.

Vinck, M., van Wingerden, M., Womelsdorf, T., Fries, P., Pennartz, C.M.A., (2010). The pairwise phase consistency: a bias-free measure of rhythmic neuronal synchronization. Neuroimage 51, 112–122.

Vinck, M., Womelsdorf, T., Buffalo, E.A., Desimone, R., Fries, P., (2013). Attentional modulation of cell-class-specific gamma-band synchronization in awake monkey area v4.

bioRxiv preprint doi: https://doi.org/10.1101/054288; this version posted May 27, 2016. The copyright holder for this preprint (which was not certified by peer review) is the author/funder. All rights reserved. No reuse allowed without permission.

Neuron 80, 1077–1089.
von Stein, A., Chiang, C., König, P., (2000). Top-down processing mediated by interareal synchronization. Proc. Natl. Acad. Sci. USA 97, 14748–14753.
Welch, P., (1967). The use of fast Fourier transform for the estimation of power spectra: A method based on time averaging over short, modified periodograms. IEEE Trans. Audio Electroacoust. 15, 70–73.
Womelsdorf, T., Fries, P., Mitra, P.P., Desimone, R., (2006). Gamma-band synchronization in visual cortex predicts speed of change detection. Nature 439, 733–736.
Wyart, V., Tallon-Baudry, C., (2008). Neural dissociation between visual awareness and spatial attention. J. Neurosci. 28, 2667–2679.

bioRxiv preprint doi: https://doi.org/10.1101/054288; this version posted May 27, 2016. The copyright holder for this preprint (which was not certified by peer review) is the author/funder. All rights reserved. No reuse allowed without permission.

Figure 1. Behavioral Task, Recording Locations, and High Resolution Spectra

(A) The task commenced with a fixation period followed by the presentation of two differently colored stimuli. The fixation point color then indicated the visual stimulus to covertly attend in either the visual hemifield ipsilateral (ipsi) or contralateral (contra) to the recording grid.

(B) Recording sites for areas V1/V2 (red), V4 (blue), and 7A (yellow) from monkey K (white spheres) and monkey P (black spheres), co-registered to a common macaque template.

(C and E) LFP-LFP PPC for 7A-V1 (C) and V1-V4 (E) during fixation (dark shading) and stimulation (light shading), averaged over all respective site pairs of monkey K. Gray bars indicate frequency regions with significant condition differences ($p<0.05$, two-tailed non-parametric randomization test, corrected for comparisons across multiple frequencies). Inset brackets denote the minimum separation required for significance. Error bars show ±1 standard error of the mean (SEM) over site pairs. Frequencies from 45 – 55 Hz were omitted due to line-noise pollution.

(D and F) Same as (C and E), but averaged over both monkeys after alignment to their beta and gamma peak frequencies.

(G and I) GC influence for 7A→V1 (G) and V1→V4 (I) during attention to the contralateral hemifield (light shading) and to the ipsilateral hemifield (dark shading), averaged over all site pairs of monkey K. Same statistics conventions as C and E.

(H and J) Same as (G and I), but averaged over both monkeys after alignment to their beta and gamma peak frequencies.

(K) Top-down modulatory stream shown by the blue arrow from 7A→V1, and bottom-up feedforward path from V1→V4 shown by the green arrow.

(L and N) Bidirectional GC influences for 7A-V1 (L) and V1-V4 (N), averaged over all site pairs of monkey K. For 7A-V1, top-down influences are shown in blue shading, and bottom-up influences in dark shading. For V1-V4, bottom-up influences are shown in green shading, and top-down influences in light shading. Same statistical conventions as C and E, but with the statistical distribution based on a non-parametric bootstrap procedure.

(M and O) Same as (L and N), but averaged over both monkeys after alignment to their beta and gamma peak frequencies.

Figure 2. Jackknife Correlation

(A) The 4 colored panels show JC averaged over all 7A→V1→V4 triplets for monkey K. The frequencies of 7A→V1 GC are shown on the vertical axis, the frequencies of V1→V4 GC are shown on the horizontal axis. The frequency ranges 1-50 Hz and 51-100 Hz are shown separately, because they required slightly different spectral analyses (see Experimental Procedures). Non-significant regions are partially masked by white ($p>0.01$, two-tailed non-parametric randomization test, corrected for multiple comparisons across both frequency axes). The line plots at the bottom show the GC spectra (±1 SEM) averaged over all V1→V4 site pairs. The line plots to the left show the GC spectra (±1 SEM) averaged over all 7A→V1 site pairs. Dashed lines mark the top-down beta GC spectral peak and the bottom-up gamma GC spectral peak.

(B) Same as (A) but averaged over both monkeys after aligning to the beta and gamma GC peak frequencies.

(C) Same as lower right color-panel in (A), but for an example triplet from monkey K showing a strong JC between 7A→V1 GC and V1→V4 GC. As in (A), dashed lines mark the GC spectral peaks. Due to more noisy spectra for this single example, peaks were found by a specialized algorithm (findpeaksG.m by T.C O'Haver).

bioRxiv preprint doi: https://doi.org/10.1101/054288; this version posted May 27, 2016. The copyright holder for this preprint (which was not certified by peer review) is the author/funder. All rights reserved. No reuse allowed without permission.

Figure 3. Spatial Specificity of Correlation Between Top-down Beta and Bottom-up Gamma GC.

(A) Inset: MRI of monkey K with the surgical trepanation and prominent sulci overlayed. The blow-up shows recording sites in 7A (yellow), V1 (red), and V4 (blue) that were analyzed. The V1 site marked by the arrow serves as an example to demonstrate the distance intervals from which another V1 site may have been chosen, which were 0 to 1 cm (magenta), 0.25 to 1.25 cm (orange), 0.5 to 1.5 cm (yellow), 0.75 to 1.75 cm (green), and 1 to 2 cm (cyan). Solid circles mark the average distance between V1 sites that were chosen for each distance interval. The particular arrangement of the distance intervals was chosen solely for the purpose of illustration.

(B) Average jackknife correlation over a ± 5 Hz window around the top-down beta and bottom-up gamma GC peak frequencies, averaged over triplets, and monkeys. The solid black circle shows the result for triplets, i.e. where the top-down beta and bottom-up gamma GC influences are connected through the same V1 site. As the distance between V1 sites increases, there is a monotonic falloff in the correlation coefficient. The mean distance between V1 sites is color-coded as solid circles matching the mean distances of the five distance intervals shown in A.

Figure 4. Lagged Jackknife Correlation (LJC) Analysis

(A) Average LJC across triplets at the top-down beta and bottom-up gamma peak GC frequencies for monkey K over ± 0.5 s lag. The blue dashed line denotes the significance level ($p=0.05$, two-tailed non-parametric randomization test) of the LJC. A dashed black line is drawn at zero lag. The green vertical line indicates the lag of the maximum LJC value, with ± 1 SEM in red. The lag of the peak LJC value is significantly different from zero ($t(3943) = -3.438$, $p<<0.001$, two-tailed).

(B) Same format as in (A), but for monkey P. The lag of the peak LJC value is significantly different from zero ($t(6719) = -6.381$, $p<<0.001$, two-tailed).

(C) Same format as in (A), but for both monkeys combined. The lag of the peak LJC value is significantly different from zero ($t(10663) = -7.576$, $p<<0.001$, two-tailed).

bioRxiv preprint doi: https://doi.org/10.1101/054288; this version posted May 27, 2016. The copyright holder for this preprint (which was not certified by peer review) is the author/funder. All rights reserved. No reuse allowed without permission.

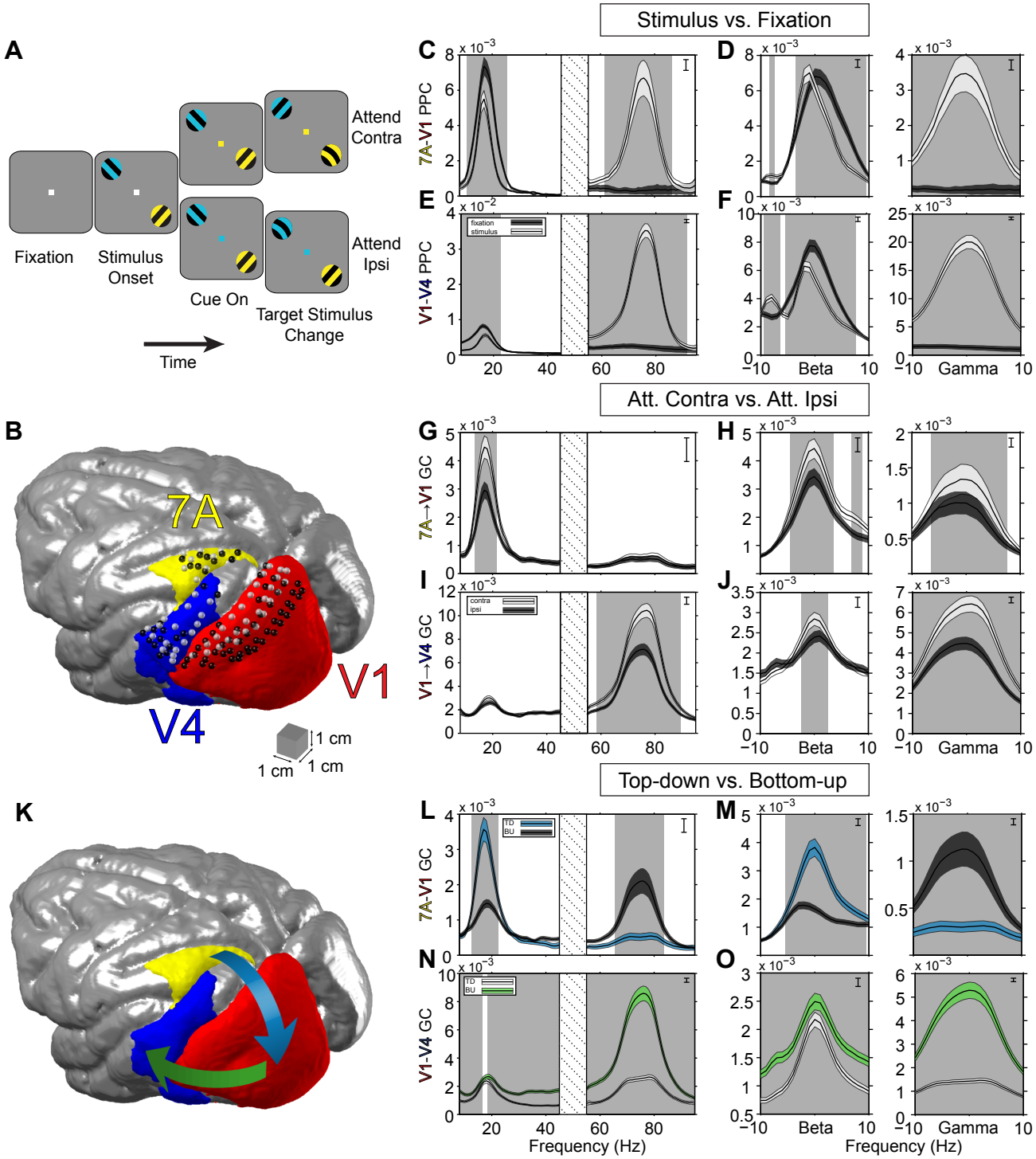

bioRxiv preprint doi: https://doi.org/10.1101/054288; this version posted May 27, 2016. The copyright holder for this preprint (which was not certified by peer review) is the author/funder. All rights reserved. No reuse allowed without permission.

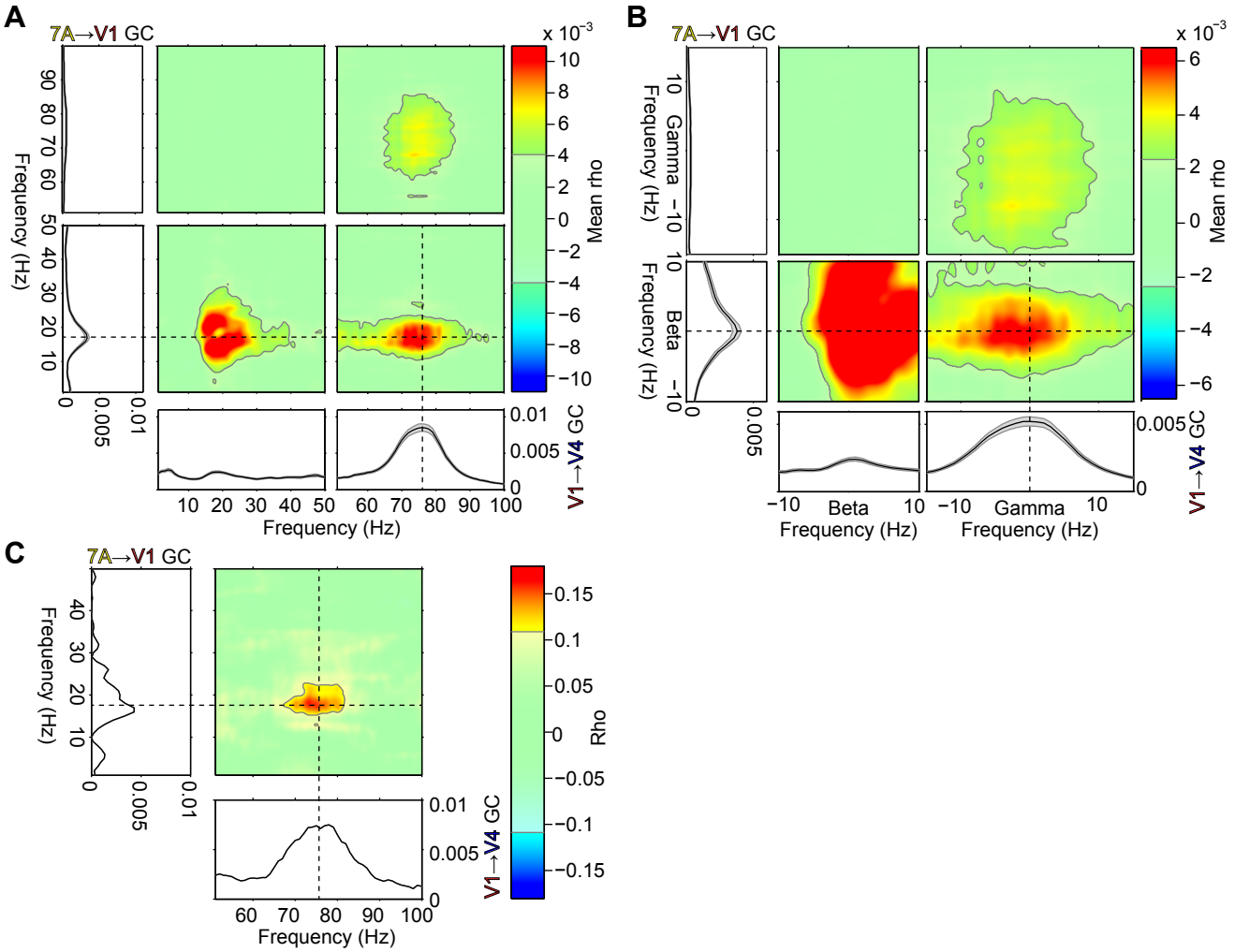

bioRxiv preprint doi: https://doi.org/10.1101/054288; this version posted May 27, 2016. The copyright holder for this preprint (which was not certified by peer review) is the author/funder. All rights reserved. No reuse allowed without permission.

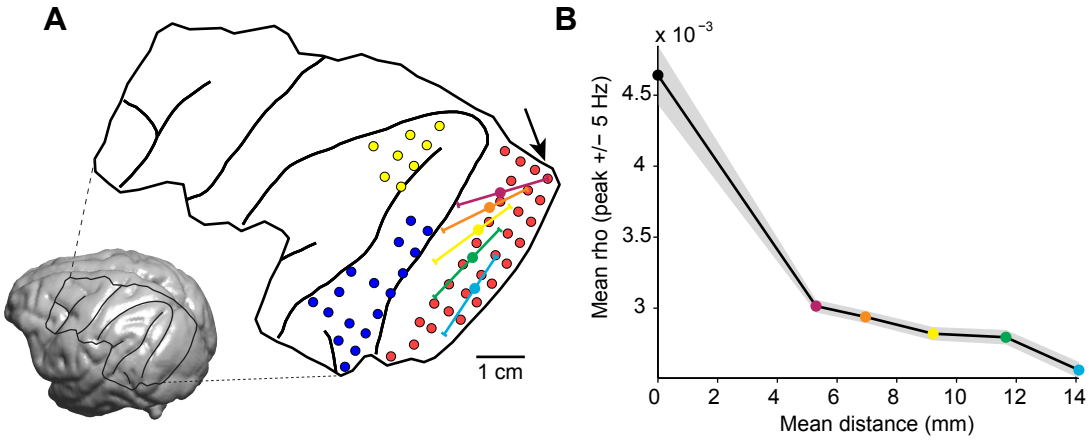
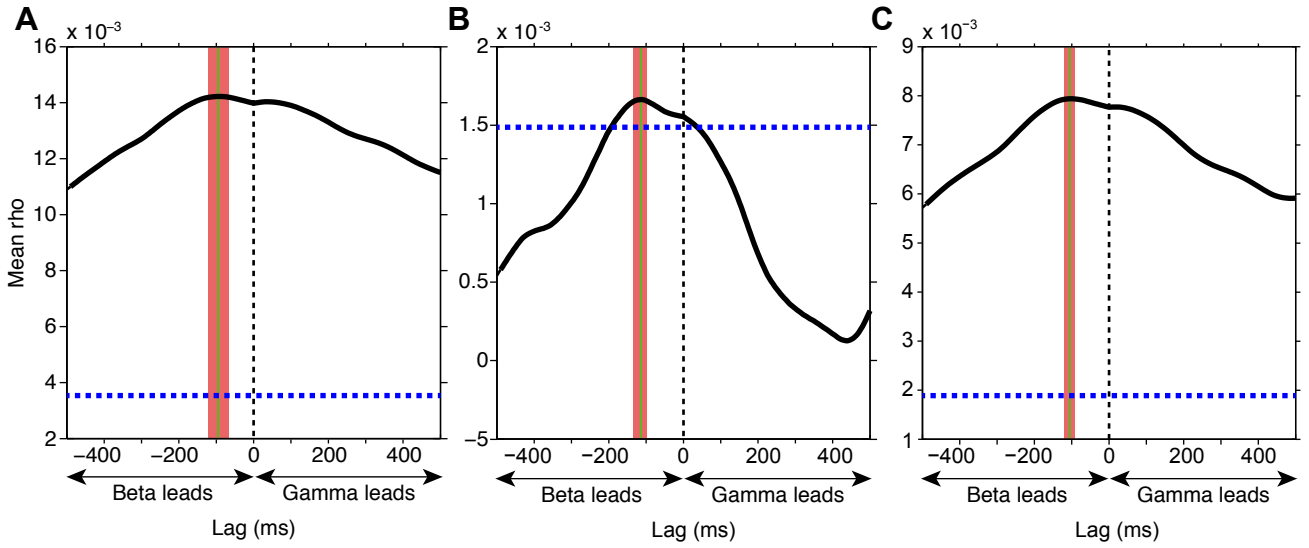
bioRxiv preprint doi: https://doi.org/10.1101/054288; this version posted May 27, 2016. The copyright holder for this preprint (which was not certified by peer review) is the author/funder. All rights reserved. No reuse allowed without permission.